APPLIED SCIENCES AND ENGINEERING

Enhanced photovoltaic performance and stability with a new type of hollow 3D perovskite {en}$FASnI_3$

Weijun Ke,[1] Constantinos C. Stoumpos,[1] Menghua Zhu,[1] Lingling Mao,[1] Ioannis Spanopoulos,[1] Jian Liu,[1] Oleg Y. Kontsevoi,[2] Michelle Chen,[1] Debajit Sarma,[1]* Yongbo Zhang,[1] Michael R. Wasielewski,[1] Mercouri G. Kanatzidis[1]†

Perovskite solar cells have revolutionized the fabrication of solution-processable solar cells. The presence of lead in the devices makes this technology less attractive, and alternative metals in perovskites are being researched as suitable alternatives. We demonstrate a new type of tin-based perovskite absorber that incorporates both ethylenediammonium (en) and formamidinium (FA), forming new materials of the type {en}$FASnI_3$. The three-dimensional $ASnI_3$ structure is stable only with methylammonium, FA, and Cs cations, and the bandgap can be tuned with solid solutions, such as $ASnI_{3-x}Br_x$. We show that en can serve as a new A cation capable of achieving marked increases in the bandgap without the need for solid solutions. The en introduces a new bandgap tuning mechanism that arises from massive Schottky style defects. In addition, incorporation of the en cation in the structure markedly increases the air stability and improves the photoelectric properties of the tin-based perovskite absorbers. Our best-performing {en}$FASnI_3$ solar cell has the highest efficiency of 7.14%, which is achieved for a lead-free perovskite cell, and retains 96% of its initial efficiency after aging over 1000 hours with encapsulation. Our results introduce a new approach for improving the performance and stability of tin-based, lead-free perovskite solar cells.

INTRODUCTION

The power conversion efficiency (PCE) of perovskite solar cells has increased from 3.8 to above 22% in just 5 years (*1*–*12*). Currently, the highest-efficiency perovskite solar cells are made of lead-based light absorbers; however, the toxicity of lead constitutes a serious issue that hinders the commercialization attempts of the perovskite solar cell technology. Therefore, it is imperative to reduce or eliminate Pb from these devices and replace it with other less toxic elements (*11*, *13*–*16*). An important limitation for the selection of suitable metal ions comes from the availability of the metal to form the perovskite crystal structure, which lends the semiconductors their unique properties. Halide perovskites have the $A^+M^{2+}X^-_3$ structural formula, where A^+ is a nonbonding univalent cation, M^{2+} is an octahedrally coordinated bivalent metal ion, and X^- is a monoanionic halide ion. Although several metal ions have been proposed as Pb alternatives (*17*, *18*), only Sn and Ge can form the genuine perovskite structure, because they both fulfill the coordination and charge balance prerequisites (*19*). Sn is an especially attractive candidate because its perovskite analogs have similar or even superior optical and electronic characteristics compared to those of Pb, which exhibit narrower optical bandgaps and higher charge-carrier mobilities (*4*). Since the initial studies on lead-free methylammonium tin iodide ($MASnI_3$) perovskite solar cells that reported a promising PCE of about 6% in 2014 (*20*, *21*), a few groups have successfully fabricated efficient Sn-based perovskite solar cells in the past 3 years (*22*–*28*). Lee *et al.* (*29*) reported formamidinium tin iodide ($FASnI_3$) perovskites with a regular device structure using pyrazine as an additive to achieve a PCE of 4.8%, whereas Liao *et al.* (*30*) reported efficient planar $FASnI_3$ perovskite solar cells with an inverted structure using a solvent-engineering method to achieve a PCE of 6.22%. Thus far, the efficiency of the Sn-based perovskite solar cells is low, and the stability of Sn-based perovskite solar cells is usually very poor in air. The low photovoltaic performance and poor environmental stability of the solar cells comes from the low redox potential of Sn^{2+}, which tends to oxidize to Sn^{4+} when exposed to the atmosphere (*4*).

RESULTS

Here, we report that ethylenediammonium (en) can serve as an A cation in the three-dimensional (3D) $FASnI_3$ perovskite structure to form a novel, hybrid 3D perovskite, {en}$FASnI_3$. The current understanding is that the $ASnI_3$ perovskite structure is stable only with A = MA^+, FA^+, and Cs^+ and that the only way to significantly increase the bandgap is to use solid solutions, such as $ASnI_{3-x}Br_x$ (*20*). Changes in A cation result only in small changes in the bandgap. We show that en can serve as a new cation capable of achieving bandgap increases that compare in magnitude to those of $ASnI_{3-x}Br_x$ solid solutions. With support from first-principles theoretical calculations, our experimental studies indicate that a new bandgap tuning mechanism is in effect, which is strongly linked to en's ability to create massive Schottky defects in the 3D structure. Inclusion of en also leads to an improved thin-film coverage and to an inhibition of the Sn^{2+}/Sn^{4+} oxidation process. The hybrid material displays a markedly increased photovoltaic performance and a drastically improved environmental stability compared to the neat $FASnI_3$ perovskite.

The new {en}$FASnI_3$ materials are obtained when en is used as an additive to fabricate $FASnI_3$-based perovskite solar cells. The obtained films show very unusual characteristics, such as the retention of the 3D crystal structure of $FASnI_3$ with increasing amounts of en, showing only a small lattice expansion. In a series of parallel experiments, we synthesized bulk samples of several {en}$FASnI_3$ compositions in concentrated hydroiodic acid (HI). The synthesis protocol involves adding a stoichiometric mixture of FAI and en in a solution of SnI_2 to an aqueous HI/H_3PO_2 solvent mixture and varying the en ratio

[1]Department of Chemistry, Northwestern University, Evanston, IL 60208, USA. [2]Department of Physics and Astronomy, Northwestern University, Evanston, IL 60208, USA.
*Present address: Department of Chemistry, Indian Institute of Technology Patna, Bihta 801103, India.
†Corresponding author. Email: m-kanatzidis@northwestern.edu

incrementally. Crystals with different amounts of en consistently show a 3D-like morphology (fig. S1).

The crystal structure of {en}$FASnI_3$ was determined by single-crystal x-ray diffraction (XRD) (Fig. 1A). Similar to $FASnI_3$, {en}$FASnI_3$ adopts a pseudocubic, orthorhombic unit cell, which has the *Amm*2 polar space group (*4*). The observable change caused by en is a small but constant increase in the normalized unit cell volume from 251.9 $Å^3$ in pristine $FASnI_3$ to 261.1 $Å^3$ in the 1:1 en/$FASnI_3$ nominal composition, also seen as a peak shift in the powder XRD (pXRD) patterns of the bulk materials (Fig. 1B). Given that en is too large to fit in the perovskite cage, it is remarkable to see that it is nevertheless incorporated in the 3D structure. Because the observed unit cell expansion is too small to account for the larger size of en compared to FA (the N···N distance is 3.75 Å in the trans configuration of $H_3NCH_2CH_2NH_3^{2+}$ in the enI_2 salt) (*31*), this suggests that certain neutral fragments of suitable size must be removed from the structure instead. These are defined as Schottky defects or, if charged $\{SnI\}^+$ species are removed in place of en (2^+), as point defects. Single-crystal refinements show that the occupancy of the Sn site is progressively reduced with increasing amounts of en (table S1). The presence of en in the structure is confirmed by proton nuclear magnetic resonance (^{1}H NMR) (Fig. 1C). Crystals and films of {en}$FASnI_3$ materials can be dissolved in dimethyl sulfoxide (DMSO)–d_6, and the en signals are accurately quantified against the FA signals. The exact ratio of FA and en in the material can be extracted from the comparison between the –CH_2– protons of en [quintuplet at δ = 3.0 parts per million (ppm)] and the –CH– proton of FA (nonaplet at δ = 7.8 ppm). The significant overlap between the –NH_3 protons from en (singlet at δ = 7.7 ppm) and the –CH– protons from FA was addressed by also including the resonant =NH_2 (singlet at δ = 9.0 ppm) and –NH_2 (doublet at δ = 8.6 ppm) protons from FA in the analysis (Fig. 1C). The en/FA ratios determined by the NMR measurements are shown in table S2. The presence of en in $FASnI_3$ is also supported by thermogravimetric analysis (TGA) data (Fig. 1D and fig. S2), showing an increasing mass loss with increasing en incorporation at the ~300°C step, which corresponds to the loss of FAI and enI_2 from the thermal decomposition of the perovskite. The loss of en at a high temperature indicates that, within the perovskite lattice, en exists in its (+2) form rather than its neutral en (0) form, which has a boiling point of ~116°C.

The optical properties of the {en}$FASnI_3$ materials are intriguing. Both the absorption and emission spectra, extracted from diffuse

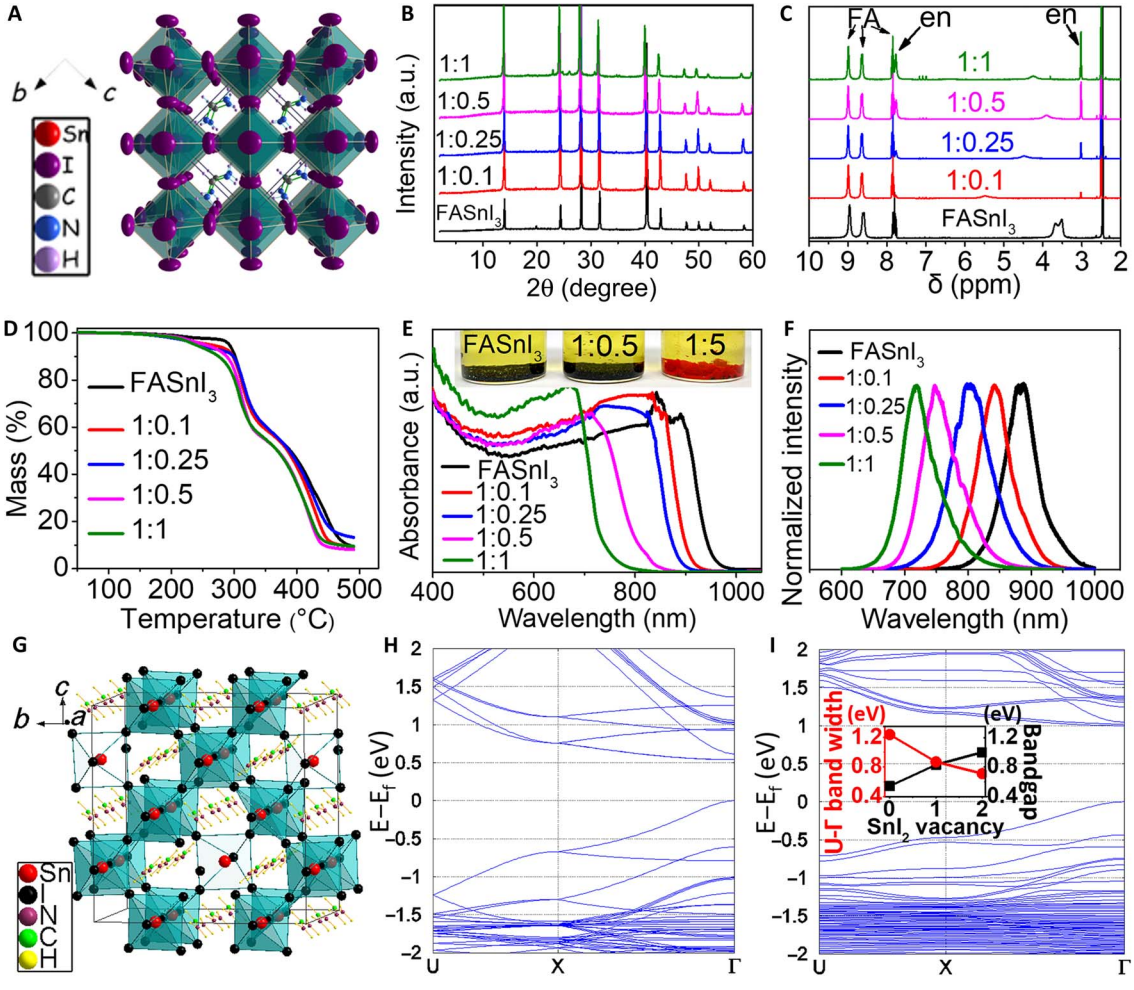

Fig. 1. Characterization of bulk materials and theory calculations. (**A**) Unit cell and crystal structure of {en}$FASnI_3$ perovskite absorber. (**B**) pXRD patterns, (**C**) ^{1}H NMR, (**D**) TGA data, (**E**) optical absorption, and (**F**) photoluminescence (PL) spectra of the {en}$FASnI_3$ perovskite crystals with various molar ratios of FA and en. a.u., arbitrary unit. (**G**) A 2 × 2 × 2 supercell of $(FA)_2Sn_2I_6$ depicting a model of the hollow perovskite with two SnI_2 vacancies [$(FA)_{16}Sn_{14}I_{44}$]. The calculated band structures of the supercell for the full [$(FA)_{16}Sn_{16}I_{48}$] and hollow [$(FA)_{16}Sn_{14}I_{44}$] perovskites are shown in (**H**) and (**I**), respectively. (I) Inset: Plot of the increase in the bandgap and decrease of the bandwidth as a function of SnI_2 vacancies in $FASnI_3$.

reflectance measurements of the bulk materials (Fig. 1E), and the PL emission spectra, obtained from crystals (Fig. 1F), show a large blue shift of the absorption edges and emission maxima with increased en loading. The blue shift trend suggests an opening of the bandgap E_g from ~1.3 eV in the black $FASnI_3$ perovskite all the way to ~1.9 eV for the 5:1 en/$FASnI_3$ molar ratio, resulting in an obvious color change from black to red (Fig. 1E, inset). The observed blue shift in the bandgap of a 3D perovskite with the $[SnI_3]^-$ perovskite is striking and cannot be explained by a simple A cation replacement in which en and FA occupy the cage space in the structure. This marked blue shift is observed only in solid solutions of $ASnI_{3-x}Br_x$ (*20*). Therefore, to increase the gap to such a large extent while keeping the 3D motif and a full iodide structure, the widths of the valence band (VB) and conduction band (CB) will have to be narrowed.

To account for the marked changes of the optical properties, we invoked the "hollow perovskite" concept based on the presence of massive Schottky defects (Fig. 1G) (*32*). If neutral fragments of SnI_2 are missing from the 3D structure, a hollow structure will emerge. This locally fragmented perovskite will feature several broken Sn-I bonds in a nonperiodic fashion so that the average structure is a pseudocubic lattice. The elimination of neutral fragments leads to a "hollow" 3D $[SnI_3]^{1-}$ network, with the degree of "hollowness" increasing with an increasing en/FA ratio. The orbital overlap among the remaining Sn/I atoms is reduced, and as a consequence, the widths of the VB and CB in this hollow structure narrow, thereby producing the experimentally observed increase in the bandgap. This exact picture is captured by density functional theory (DFT) calculations for a $2 \times 2 \times 2$ supercell, where SnI_2 units have been removed (Fig. 1, G to I). DFT calculations directly point to the reduction of the bandwidths upon structural relaxation, with the VB showing a much larger decrease than the CB. The calculated bandgaps increase proportionally with the number of missing SnI_2 units, in agreement with the experimentally observed trend in the bandgaps of {en}$FASnI_3$ (Fig. 1, H and I). The decrease of the energy levels of the VB maxima upon extrusion of SnI_2 units has further implications in the stability of the perovskite because the absolute work function is shifted to lower energy, and as a result, the tendency of the materials to undergo oxidation diminishes. The model of the hollow perovskite is fully supported by the lower observed mass densities of the {en}$FASnI_3$ materials, as determined by gas pycnometry. The mass density decreases with an increasing en/FA ratio, and for any given composition, the experimentally measured density is consistently smaller than the theoretically predicted one, assuming full atom occupancy in the crystal structure (Table 1 and table S3). On the basis of the above, we propose that {en}$FASnI_3$ is an entirely new type of 3D perovskite that is very different from the classical $ASnI_{3-x}Br_x$ and $APbI_{3-x}Br_x$ systems.

Having established the fundamental properties of the new perovskites, we proceeded in casting thin films. One of the major problems associated with the successful fabrication of Sn films comes from the difficulty of preparing high-quality, high-coverage thin films. Many different approaches to film deposition have been reported to improve the film quality, including thermal evaporation (*33*, *34*), vapor-assisted deposition (*23*, *35*), and solvent engineering methods (*28*–*30*, *36*). These methods, which normally involve complex processes that limit large-scale fabrication, are not necessary because {en}$FASnI_3$ forms highly uniform films using the simple one-step method. Figure 2 (A and B) shows scanning electron microscopy (SEM) images comparing perovskite films prepared with $FASnI_3$ (Fig. 2A) and {en}$FASnI_3$ (Fig. 2B) using the one-step method. All the films used in this study include 15% SnF_2 as an additive to reduce the background hole carrier density and improve the solar cell performance (*24*). As shown in Fig. 2A, the film coverage is poor for the $FASnI_3$ film because of its fast crystallization. In stark contrast, the {en}$FASnI_3$ film is much smoother with less pinholes after adding 10% en in the precursor solution (Fig. 2B). The effect is consistent for several {en}$FASnI_3$ perovskite films with variable en loadings (fig. S3).

Table 1. Comparison of experimental and theoretical crystal densities of all reported materials, along with SD.

Material/density (g cm^{-3})	Experiment	Single crystal (full occupancy)	Single crystal (Sn-refined)
$FASnI_3$	3.594(1)	3.604(3)	3.596(3)
1:0.1	3.479(1)	3.587(3)	3.565(3)
1:0.25	3.459(1)	3.547(3)	3.497(3)
1:0.5	3.403(1)	3.536(3)	3.467(3)
1:1	3.285(1)	3.507(3)	3.386(3)

The actual composition of {en}$FASnI_3$ agrees with the stoichiometric addition of en to the precursor solution. To quantify the amount of en in the perovskite films, we measured the ^{1}H NMR spectra of the perovskite films prepared by the precursor with 0, 10, and 100% en, as shown in fig. S4. It can be estimated that the molar ratio of en and FA in the final film is very close to that in the precursor. The overall agreement is established by comparing the XRD patterns (Fig. 2C) and optical absorption (Fig. 2D). Figure 2C shows the XRD patterns of the perovskite films coated on mesoporous TiO_2 with and without en. The films with en exhibit a shift of the Bragg reflections to smaller 2θ angles compared with the neat $FASnI_3$ film, suggesting an increase in the unit cell volume. The parameters in the {en}$FASnI_3$ film agree with the XRD results of the bulk materials. Similar with the bulk materials, the absorption spectra of the {en}$FASnI_3$ films show the same marked difference in bandgap. Figure 2D shows the optical absorption spectra of the {en}$FASnI_3$ perovskite films with 0, 10, and 25% en loading. The absorption wavelength systematically decreases with an increased en/FA ratio, and the absorption edge becomes sharper, suggesting that the optical absorption coefficient increases. The estimated bandgaps of the perovskite absorbers with 0, 10, and 25% en are 1.4, 1.5, and 1.9 eV, respectively (fig. S5).

Figure 2E shows the PL spectra of the perovskite films of {en}$FASnI_3$ with various amounts of en deposited on mesoporous TiO_2. The neat $FASnI_3$ perovskite film displays a typical emission peak at about 870 nm. The {en}$FASnI_3$ perovskite films with 10 and 25% en/FA ratio display emission peaks at about 840 and 760 nm, respectively. The blue-shifted emission spectra are consistent with the results obtained from UV-vis absorption of the films. Figure 2F shows the TRPL spectra of the {en}$FASnI_3$ perovskite films. The neat $FASnI_3$ perovskite film has an estimated carrier lifetime of 0.19 ns. In contrast, the carrier lifetime of the perovskite films with 10 and 25% en loading are 0.46 and 0.68 ns, respectively. The longer carrier lifetime of the films with en loading can be mainly attributed to the better film quality, as shown in Fig. 2 (A and B).

Figure 3A shows a cross-sectional SEM image of a completed solar cell using a perovskite absorber with 10% en loading. We can observe the two layers between the Au electrode and the fluorine-doped tin oxide (FTO) by blocking TiO_2: a 150-nm-thick capping layer of

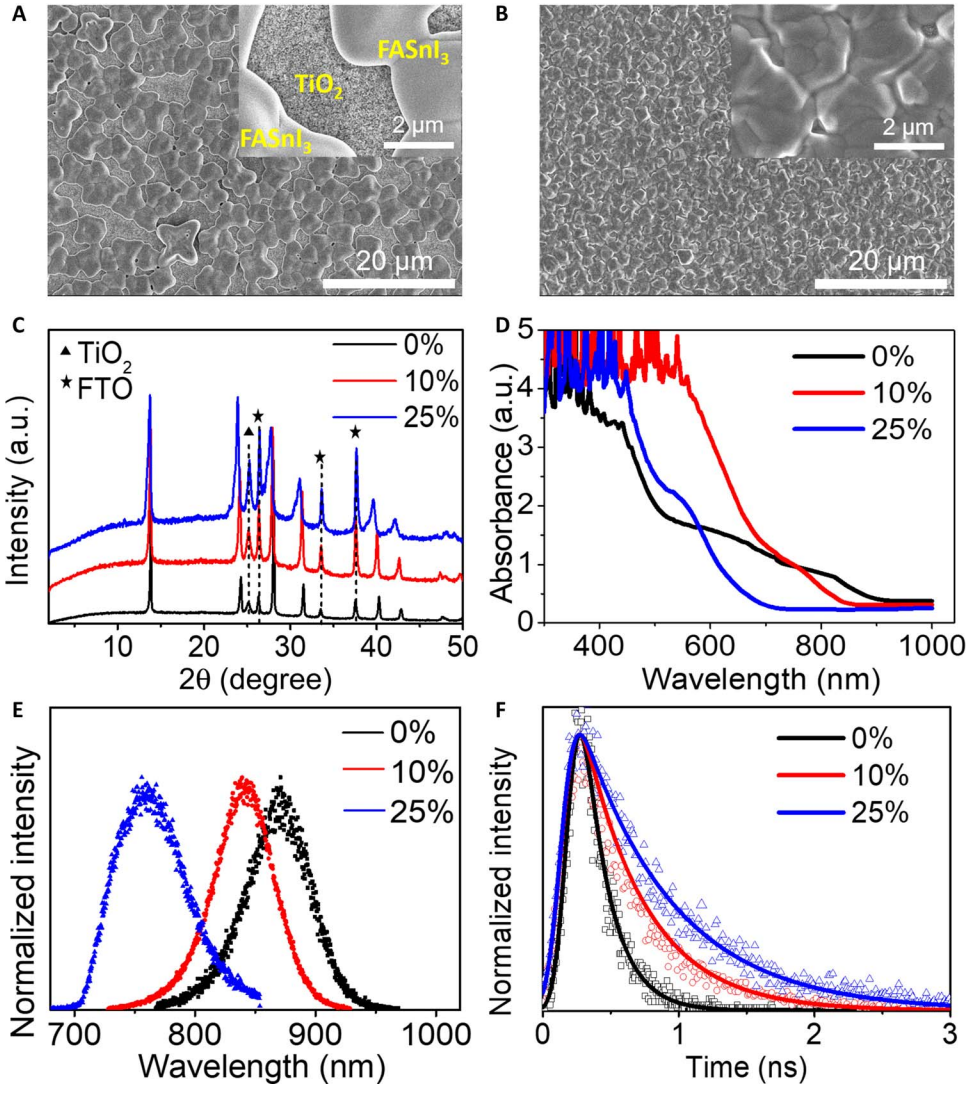

Fig. 2. Characterization of films. Top-view SEM images of the perovskite films (**A**) without and (**B**) with 10% en loading deposited on the mesoporous TiO_2 at low magnification. Insets: Top-view SEM images of the same films at high magnifications. (**C**) XRD patterns, (**D**) ultraviolet-visible (UV-vis) absorption, (**E**) PL, and (**F**) time-resolved PL (TRPL) spectra of the perovskite films with various amounts of en loading deposited on mesoporous TiO_2.

{en}$FASnI_3$ with a thin poly[bis(4-phenyl)(2,4,6-trimethylphenyl) amine] (PTAA) hole-transporting layer and a 1-μm-thick mesoporous TiO_2 layer infiltrated with a perovskite absorber. We then investigated the effect of en on the solar cell performance. Figure 3B shows the photocurrent density-voltage (*J-V*) curves of three representative solar cells using the perovskite absorbers with 0, 10, and 25% en loading. The neat $FASnI_3$ perovskite solar cell achieved a relatively low PCE of 1.40% with a V_{oc} (open-circuit voltage) of 0.15 V, a J_{sc} (short-circuit current density) of 23.76 mA cm^{-2}, and an FF (fill factor) of 38.24% when measured under the reverse voltage scan (that is, from V_{oc} to 0 V). This poor performance can be attributed to poor film coverage and serious recombination inside the perovskite absorber. However, the solar cell performance is significantly improved when using {en}$FASnI_3$ as the absorber. The material with 10% en loading achieved a high PCE of 6.94% with a V_{oc} of 0.47 V, a J_{sc} of 22.29 mA cm^{-2}, and an FF of 66.41% when measured under the reverse voltage scan. There is a significant enhancement in V_{oc} and FF, whereas the J_{sc} values of the devices using the perovskite with and without en are comparable. The solar cells use the perovskite absorber with 25% en loading, yielding a PCE of 2.34% with a high V_{oc} of 0.55 V, a J_{sc} of 7.64 mA cm^{-2}, and an FF of 55.80% under the same measurement conditions. As the en loading increases, the solar cells achieve a higher V_{oc}, but the obtained J_{sc} is lower, a trend that can probably be attributed to the much wider bandgap (up to 1.9 eV) and worse carrier transport. Therefore, the amount of en loading in the {en}$FASnI_3$ is critical to the device performance. To optimize the amount of en addition, we fabricated the perovskite films with 7.5, 10, 12.5, and 15% en loading. The optical absorption spectra of the {en}$FASnI_3$ films, the *J-V* curves measured under the reverse voltage scan, and the external quantum efficiency (EQE) curves of the {en}$FASnI_3$ solar cells with various amounts of en addition are shown in fig. S6 (A, B, and C, respectively). The photovoltaic parameters of the solar cells using the perovskite absorbers with various amounts of en addition are summarized in table S4. We found that the optimum device performance was obtained from the sample with the perovskite absorber with 10% en loading.

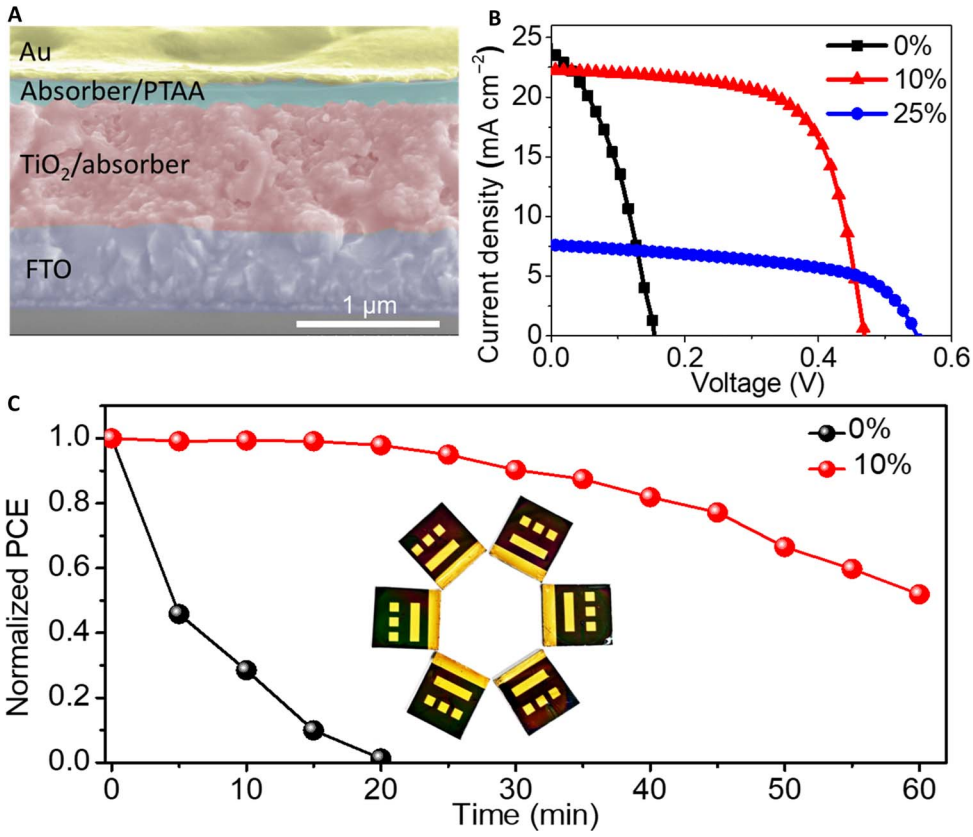

Fig. 3. Performance and stability of devices. (**A**) Cross-sectional SEM image of a completed device. (**B**) *J-V* curves of the solar cells using the perovskite absorbers with various amounts of en addition. (**C**) Aging test on the unencapsulated solar cells with and without 10% en under constant AM1.5G (air mass 1.5 global) illumination in ambient air.

To evaluate the stability of the {en}$FASnI_3$ perovskite absorber toward moisture and oxygen, we exposed the unencapsulated films (neat and with 10% en loading) to ambient air. Figure S7A shows that the absorption of the classical $FASnI_3$ perovskite film was significantly reduced because of serious degradation after exposure for 6 hours. In contrast, the {en}$FASnI_3$ perovskite film exhibits much better stability over the same period under the same conditions, as shown in fig. S7B. The improved stability of the film was further confirmed by XRD. The XRD patterns of the pure $FASnI_3$ perovskite film degraded after they were exposed to ambient air for 6 hours (fig. S7, C and E). However, the XRD patterns of the {en}$FASnI_3$ film are stable (fig. S7, D and F) and agree with the optical absorption results. We also tested the thermal stability of the perovskite films. As shown in fig. S8, the film with en loading exhibits much better thermal stability than does the neat $FASnI_3$ film. The neat film was almost decomposed and became transparent after it was annealed in ambient air for 40 min at 100°C. In contrast, the film with 10% en remained black when treated under the same conditions. We then investigated the durability of device performance as a function of time under constant AM1.5G illumination in air at room temperature (Fig. 3C). The plot shows that the unencapsulated solar cell with the classical $FASnI_3$ absorber degraded rapidly, and after 20 min, the efficiency decreased from 1.28 to 0% (short circuit). However, the unencapsulated {en}$FASnI_3$ device with 10% en retained 50% of its initial efficiency of 6.23% under the same conditions.

Figure 4A shows the *J-V* curves of the best-performing solar cell using the perovskite absorber with 10% en, measured under reverse and forward voltage scans. This solar cell achieved a PCE of 7.14% with a V_{oc} of 0.480 V, a J_{sc} of 22.54 mA cm^{-2}, and an FF of 65.96% when measured under the reverse voltage scan and a PCE of 6.90% with a V_{oc} of 0.475 V, a J_{sc} of 22.54 mA cm^{-2}, and an FF of 64.47% when measured under the forward voltage scan, showing a small hysteresis. Figure 4B shows the measured EQE spectrum of the solar cell using the perovskite absorber with 10% en, displaying a high average value in the 300- to 850-nm wavelength range, which is consistent with the absorption spectrum of the {en}$FASnI_3$ perovskite with 10% en loading. The integrated J_{sc} calculated from the EQE curve is about 22.29 mA cm^{-2}, which is very close to the J_{sc} obtained from the *J-V* measurements. Figure 4C shows the histograms of PCEs for 60 solar cells with 10% en. The average V_{oc}, J_{sc}, FF, and PCE are 0.43 ± 0.02 V, 21.90 ± 1.13 mA cm^{-2}, 63.83 ± 2.16%, and 6.05 ± 0.46%, respectively, showing high average performance and a good reproducibility of our {en}$FASnI_3$ perovskite solar cells. To evaluate the stabilized power output of the {en}$FASnI_3$ device, we measured the photocurrent of a typical device with 10% en at a maximum power voltage of 0.333 V, showing a steady-state PCE of 6.65% with a steady-state current density of 19.98 mA cm^{-2} (fig. S9). Because the uniform {en}$FASnI_3$ film can be obtained by the simple one-step method, we also fabricated solar cells with a larger active area. Figure S10 (A and B) shows that the solar cells using the {en}$FASnI_3$ absorbers (10% en) with active areas of 0.39 and 1.1 cm^2 achieved PCEs of 6.09 and 4.30%, respectively. Finally, we check the long-term stability of our {en}$FASnI_3$ device. Figure 4D shows that our encapsulated device is very stable and maintains an efficiency of ~6.37% even after 1000 hours.

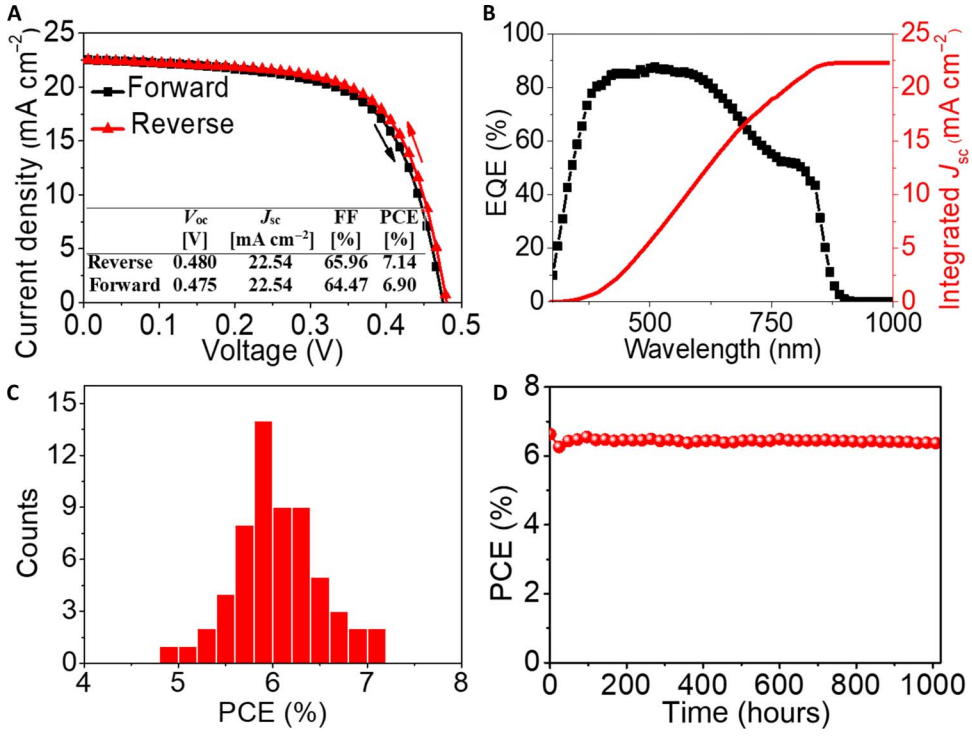

Fig. 4. Performance of the champion device and reproducibility and stability of devices. (**A**) *J-V* curves of the best-performing solar cell using an {en}$FASnI_3$ perovskite absorber with 10% en loading measured under reverse and forward voltage scans. (**B**) EQE and integrated J_{sc} measured from a solar cell with 10% en. (**C**) Histograms of PCEs for 60 solar cells with 10% en. (**D**) Efficiency of an encapsulated device with 10% en as a function of the storage time.

DISCUSSION

We have shown that en can be incorporated into the $FASnI_3$ perovskite structure to stabilize the new perovskite variety of {en}$FASnI_3$, which has a hollow structure with randomly distributed Schottky defects. When used as a solar absorber, {en}$FASnI_3$ shows excellent semiconducting properties, such as tunable bandgap and reduced background carrier density, resulting in significantly enhanced performance and environmental stability for lead-free solar cells. The best-performing solar cell using the perovskite absorber with 10% en loading achieved a PCE of 7.14% with a V_{oc} of 0.480 V, a J_{sc} of 22.54 mA cm^{-2}, and an FF of 65.96%. The significantly improved efficiency and stability compared to neat $FASnI_3$ makes the new {en}$FASnI_3$ perovskites very attractive for further improvement of lead-free device performance. We anticipate that this approach is applicable not only to Sn-based solar cells but also to lead-based perovskite solar cells and devices.

MATERIALS AND METHODS

Preparation of materials and thin films

The method of growing perovskite crystals with and without en was adopted from Stoumpos *et al.* (*4*). $SnCl_2{\cdot}2H_2O$ (3 mmol; 98%, Sigma-Aldrich) with various amounts of en (0 to 3 mmol) was dissolved in a mixture of 57% (w/w) aqueous HI solution (5.1 ml) and 50% aqueous H_3PO_2 (1.7 ml) by heating to boiling under constant magnetic stirring for about 5 min, which formed a bright yellow solution. Formamidine acetate salt (3 mmol; ≥98.0%, Sigma-Aldrich) was subsequently added to the hot yellow solution, and stirring was continued for 10 min. Then, the solution was left to cool to room temperature, and the crystals were collected by suction filtration and dried in a vacuum oven for 12 hours at 125°C. For the red sample with a molar ratio of 1:5, the synthesis process was the same except for the molar concentration (1 mmol of $SnCl_2{\cdot}2H_2O$, 5 mmol of en, and 1 mmol of formamidine acetate salt).

The preparation of compact and mesoporous TiO_2 layers on FTO has been reported elsewhere (*37*). First, a compact TiO_2 layer was spin-coated onto an FTO substrate (TEC 15, Hartford Glass) from an ethanol solution of titanium isopropoxide at 2000 rpm for 30 s and then annealed in air for 20 min at 500°C. Subsequently, a mesoporous TiO_2 layer composed of 20-nm particles (Dyesol DSL 18NR-T) was spin-coated onto the compact layer using a diluted solution in anhydrous ethanol (1:3.5 weight ratio) at 500 rpm for 1 min and then annealed in air for 15 min at 500°C. Finally, the annealed mesoporous TiO_2 film was dipped into a 0.02 M aqueous $TiCl_4$ solution for 30 min at 70°C and then annealed for 15 min at 500°C. For the film fabrication, the $FASnI_3$ precursor solution, consisting of 409.8 mg of homemade SnI_2 (*4*), 172 mg of FAI (Dyesol), and 24 mg of SnF_2 (99%, Sigma-Aldrich), was dissolved in 632.8 μl of *N*,*N*-dimethylformamide and 70.8 μl of DMSO. After all the materials were dissolved, 4.8, 6.4, 8, 9.6, and 16 μl of en (≥99%, Sigma-Aldrich) were added to the solution for the precursors with 7.5, 10, 12.5, 15, and 25% en, respectively. The precursors with or without en addition were spin-coated on the mesoporous layers with a spin rate of 1500 rpm for 60 s. The substrates were annealed for 5 min at 70°C and then for 10 min at 120°C on a hot plate. The solution of hole-transporting material, consisting of 32 mg of PTAA (99%, Sigma-Aldrich) and 3.6 mg of 4-isopropyl-4′-methyldiphenyliodonium tetrakis(pentafluorophenyl)borate (TCI America) in 1.6 ml of chlorobenzene,

was spin-coated on the perovskite films at 1500 rpm for 30 s and then annealed for 5 min at 70°C. All these procedures were performed in a glove box with very low oxygen and moisture levels, which are about 0 to 5 ppm and beyond the detection limits of the system. To complete the device, a 100-nm-thick Au electrode was thermally evaporated on top of the hole-transporting layer with a metal mask. The active area of the solar cells was 0.09, 0.39, or 1.10 cm^2.

Electronic band structure calculations

First-principles electronic band structure calculations were carried out within the DFT formalism using the projector augmented-wave method (*38*) implemented in the Vienna Ab initio Simulation Package (*39*). The initial configuration was represented by the 2 × 2 × 2 supercell of the conventional orthorhombic unit cell [$(FA)_2Sn_2I_6$ composition] of $FASnI_3$, corresponding to the lowest energy structure of $FASnI_3$ (*40*). The two hollow perovskite structures were constructed from the same supercell of $FASnI_3$ by removing one or two SnI_2 units, creating vacancy sites. The compositions of the initial perovskite structure and of the structures with one and two SnI_2 vacancies were $(FA)_{16}Sn_{16}I_{48}$, $(FA)_{16}Sn_{15}I_{46}$, and $(FA)_{16}Sn_{14}I_{44}$, respectively. The internal atomic positions were optimized until the atomic forces on each atom were less than 0.01 eV $Å^{-1}$, with a plane-wave cutoff energy of 350 eV and a 4 × 3 × 3 Γ-centered Monkhorst-Pack k-point grid, whereas the volume and shape of the unit cell were fixed. Multiple possible orientations of SnI_2 vacancies in the single-vacancy supercells and mutual configurations of SnI_2 vacancies in two-vacancy supercells were considered, and lowest-energy configurations were selected for further band structure analysis. For the exchange-correlation function, the generalized gradient approximation was used within Perdew-Burke-Ernzerhof (PBE) formalism (*41*). A well-known tendency of a semilocal PBE functional is to underestimate the bandgaps compared to experimentally obtained values; however, it would reproduce general trends in bandgap change under uniform transformation in the same material well.

Materials, film, and device characterization

The morphology of the crystals, films, and devices was characterized by a high-resolution field- emission SEM (Hitachi SU8030). The XRD spectra of the perovskite films and crystals with and without en were obtained on a Rigaku MiniFlex600 pXRD (Cu Kα graphite, λ = 1.5406 Å) operating at 40 kV/15 mA with a Kβ foil filter. Optical diffuse reflectance measurements of the perovskite crystals and UV-vis absorption spectra of the films were performed using a Shimadzu UV-3600 UV-VIS-NIR spectrometer operating in the 200- to 2000-nm region at room temperature. $BaSO_4$ was used as a nonabsorbing reflectance reference. The generated reflectance-versus-wavelength data were used to estimate the bandgap of the material by converting the reflectance to absorbance data according to the Kubelka-Munk equation: $\alpha/S = (1 - R)^2/2R$, where R is the reflectance and α and S are the absorption and scattering coefficients, respectively (*4*). PL spectra were collected on rhombic dodecahedral crystals of {en}$FASnI_3$ using a Horiba LabRAM HR Evolution confocal Raman microscope spectrometer (600 g mm^{-1} diffraction grating) equipped with a diode continuous-wave laser (473 nm, 25 mW) and a Synapse charge-coupled device camera. The incident laser beam was parallel to the (010) direction of the crystals and focused at a ~1-μm spot size. Unless stated otherwise, the maximum power output of the laser source was filtered to 1% of the maximum power output. The ^{1}H NMR spectra of films were recorded on a 400-MHz Agilent DD2-MR400 spectrometer with a OneNMR probe and Agilent 7600 96-sample autosampler. The ^{1}H NMR spectra of crystals were recorded on the Bruker AVANCE III 600-MHz system with a BBI (broadband inverse) probe. All samples were prepared by dissolving a small portion of the dried solids (~10 mg) in 0.6 ml of DMSO-d_6 solution. Single crystals of appropriate size were selected for XRD experiments. After screening few diffraction frames to ensure crystal quality, we collected full sphere data using a STOE IPDS II diffractometer with graphite-monochromatized Mo Kα radiation (λ = 0.71073 Å), operating at 50 kV and 40 mA under N_2 flow. Integration and numerical absorption corrections on the data were performed using the STOE X-Area programs. Crystal structures were solved by direct methods and refined by full-matrix least-squares method on F^2 using the Jana2006 program package (*42*). All data were collected at room temperature under N_2 flow. TGA measurements were performed on a Netzsch simultaneous thermal analysis system. The sample (30 mg) was placed inside an alumina cap and heated from 30° to 500°C under He flow at a heating rate of 5°C min^{-1}. A Micromeritics AccuPyc II 1340 pycnometer was used for density determination of all samples. Dry sample (400 mg) was loaded to an aluminum cap (1 ml), and the volume determination was performed on the basis of He displacement. Each sample was measured five times, and the sample volume was recorded along with its SD. The average volume of each sample was used for the density calculations.

The EQE spectra were characterized by an Oriel model QEPVSI instrument equipped with a National Institute of Standards and Technology–certified Si diode. *J-V* curves were characterized by a Keithley model 2400 instrument under AM1.5G simulated irradiation with a standard solar simulator (Abet Technologies). The integration time and voltage step of the *J-V* measurements are 16.67 ms and 12.1 mV, respectively. The light intensity of the solar simulator was calibrated by a National Renewable Energy Laboratory–certified monocrystalline silicon solar cell. Steady-state efficiency was performed on a CHI electrochemical workstation. TRPL lifetimes were measured with a streak camera setup (Hamamatsu C4334 Streakscope). The instrument response function was approximately 4% of the sweep window. A commercial direct diode–pumped 100-kHz amplifier (Spirit 1040-4, Spectra-Physics) produces a fundamental beam of 1040 nm (350 fs, 4.5 W). This light was used to pump a noncollinear optical parametric amplifier (Spirit-NOPA, Spectra-Physics), which delivers high repetition rate pulses. The samples were excited with 560-nm, 0.3-nJ pulses.

SUPPLEMENTARY MATERIALS

Supplementary material for this article is available at http://advances.sciencemag.org/cgi/content/full/3/8/e1701293/DC1

fig. S1. Top-view SEM images of the {en}$FASnI_3$ crystals.
fig. S2. TGA spectra of FAI, enI_2, and SnI_2 powder.
fig. S3. Top-view SEM images of the {en}$FASnI_3$ perovskite films with various amounts of en loading.
fig. S4. ^{1}H NMR spectra of the films with and without en loading.
fig. S5. Bandgaps of the {en}$FASnI_3$ perovskite films.
fig. S6. UV-vis optical absorption spectra, *J-V*, and EQE curves of the perovskite absorbers with various amounts of en loading.
fig. S7. Air stability of UV-vis absorption spectra and XRD patterns of the {en}$FASnI_3$ perovskite films.
fig. S8. Thermal stability test of the {en}$FASnI_3$ perovskite films.
fig. S9. Steady-state efficiency of an {en}$FASnI_3$ solar cell with 10% en loading.
fig. S10. *J-V* curves of {en}$FASnI_3$ solar cells with larger active areas.
table S1. Unit cells, bonding parameters, and refinement parameters of {en}$FASnI_3$ crystals.
table S2. Comparison of the initial and final FA/en ratio on NMR and density measurements.

table S3. Comparison of experimental and theoretical crystal densities of all reported materials.
table S4. Summary of the photovoltaic parameters of the {en}$FASnI_3$ solar cells with various amounts of en loading.

REFERENCES AND NOTES

1. D. B. Mitzi, Synthesis, structure, and properties of organic-inorganic perovskites and related materials, in *Progress in Inorganic Chemistry Volume 48*, K. D. Karlin, Ed. (John Wiley & Sons Inc., 1999).
2. W. J. Yin, T. Shi, Y. Yan, Unique properties of halide perovskites as possible origins of the superior solar cell performance. *Adv. Mater.* **26**, 4653–4658 (2014).
3. S. D. Stranks, G. E. Eperon, G. Grancini, C. Menelaou, M. J. Alcocer, T. Leijtens, L. M. Herz, A. Petrozza, H. J. Snaith, Electron-hole diffusion lengths exceeding 1 micrometer in an organometal trihalide perovskite absorber. *Science* **342**, 341–344 (2013).
4. C. C. Stoumpos, C. D. Malliakas, M. G. Kanatzidis, Semiconducting tin and lead iodide perovskites with organic cations: Phase transitions, high mobilities, and near-infrared photoluminescent properties. *Inorg. Chem.* **52**, 9019–9038 (2013).
5. H.-S. Kim, C.-R. Lee, J.-H. Im, K.-B. Lee, T. Moehl, A. Marchioro, S.-J. Moon, R. Humphry-Baker, J.-H. Yum, J. E. Moser, M. Grätzel, N.-G. Park, Lead iodide perovskite sensitized all-solid-state submicron thin film mesoscopic solar cell with efficiency exceeding 9%. *Sci. Rep.* **2**, 591 (2012).
6. M. M. Lee, J. Teuscher, T. Miyasaka, T. N. Murakami, H. J. Snaith, Efficient hybrid solar cells based on meso-superstructured organometal halide perovskites. *Science* **338**, 643–647 (2012).
7. J. Burschka, N. Pellet, S.-J. Moon, R. Humphry-Baker, P. Gao, M. K. Nazeeruddin, M. Grätzel, Sequential deposition as a route to high-performance perovskite-sensitized solar cells. *Nature* **499**, 316–319 (2013).
8. H. Zhou, Q. Chen, G. Li, S. Luo, T.-b. Song, H. S. Duan, Z. Hong, J. You, Y. Liu, Y. Yang, Interface engineering of highly efficient perovskite solar cells. *Science* **345**, 542–546 (2014).
9. W. S. Yang, J. H. Noh, N. J. Jeon, Y. C. Kim, S. Ryu, J. Seo, S. I. Seok, High-performance photovoltaic perovskite layers fabricated through intramolecular exchange. *Science* **348**, 1234–1237 (2015).
10. M. Saliba, T. Matsui, K. Domanski, J.-Y. Seo, A. Ummadisingu, S. M. Zakeeruddin, J.-P. Correa-Baena, W. R. Tress, A. Abate, A. Hagfeldt, M. Grätzel, Incorporation of rubidium cations into perovskite solar cells improves photovoltaic performance. *Science* **354**, 206–209 (2016).
11. G. E. Eperon, T. Leijtens, K. A. Bush, R. Prasanna, T. Green, J. T.-W. Wang, D. P. McMeekin, G. Volonakis, R. L. Milot, R. May, A. Palmstrom, D. J. Slotcavage, R. A. Belisle, J. B. Patel, E. S. Parrott, R. J. Sutton, W. Ma, F. Moghadam, B. Conings, A. Babayigit, H.-G. Boyen, S. Bent, F. Giustino, L. M. Herz, M. B. Johnston, M. D. McGehee, H. J. Snaith, Perovskite-perovskite tandem photovoltaics with optimized bandgaps. *Science* **354**, 861–865 (2016).
12. National Renewable Energy Laboratory, "Best Research-Cell Efficiencies"; https://www.nrel.gov/pv/assets/images/efficiency-chart.png.
13. Z. Yang, A. Rajagopal, C. C. Chueh, S. B. Jo, B. Liu, T. Zhao, A. K. Jen, Stable low-bandgap Pb-Sn binary perovskites for tandem solar cells. *Adv. Mater.* **28**, 8990–8997 (2016).
14. B. Zhao, M. Abdi-Jalebi, M. Tabachnyk, H. Glass, V. S. Kamboj, W. Nie, A. J. Pearson, Y. Puttisong, K. C. Gödel, H. E. Beere, D. A. Ritchie, A. D. Mohite, S. E. Dutton, R. H. Friend, A. Sadhanala, High open-circuit voltages in tin-rich low-bandgap perovskite-based planar heterojunction photovoltaics. *Adv. Mater.* **29**, 1604744 (2017).
15. D. Zhao, Y. Yu, C. Wang, W. Liao, N. Shrestha, C. R. Grice, A. J. Cimaroli, L. Guan, R. J. Ellingson, K. Zhu, X. Zhao, R.-G. Xiong, Y. Yan, Low-bandgap mixed tin–lead iodide perovskite absorbers with long carrier lifetimes for all-perovskite tandem solar cells. *Nat. Energy* **2**, 17018 (2017).
16. Y. Kim, Z. Yang, A. Jain, O. Voznyy, G. H. Kim, M. Liu, L. N. Quan, F. P. Garcia de Arquer, R. Comin, J. Z. Fan, E. H. Sargent, Pure cubic-phase hybrid iodobismuthates $AgBi_2I_7$ for thin-film photovoltaics. *Angew. Chem. Int. Ed.* **55**, 9586–9590 (2016).
17. S. Kazim, M. K. Nazeeruddin, M. Gratzel, S. Ahmad, Perovskite as light harvester: A game changer in photovoltaics. *Angew. Chem. Int. Ed.* **53**, 2812–2824 (2014).
18. B. Saparov, D. B. Mitzi, Organic-inorganic perovskites: Structural versatility for functional materials design. *Chem. Rev.* **116**, 4558–4596 (2016).
19. C. C. Stoumpos, M. G. Kanatzidis, The renaissance of halide perovskites and their evolution as emerging semiconductors. *Acc. Chem. Res.* **48**, 2791–2802 (2015).
20. F. Hao, C. C. Stoumpos, D. H. Cao, R. P. H. Chang, M. G. Kanatzidis, Lead-free solid-state organic–inorganic halide perovskite solar cells. *Nat. Photonics* **8**, 489–494 (2014).
21. N. K. Noel, S. D. Stranks, A. Abate, C. Wehrenfennig, S. Guarnera, A.-A. Haghighirad, A. Sadhanala, G. E. Eperon, S. K. Pathak, M. B. Johnston, A. Petrozza, L. M. Herz, H. J. Snaith, Lead-free organic–inorganic tin halide perovskites for photovoltaic applications. *Energy Environ. Sci.* **7**, 3061–3068 (2014).
22. T. M. Koh, T. Krishnamoorthy, N. Yantara, C. Shi, W. L. Leong, P. P. Boix, A. C. Grimsdale, S. G. Mhaisalkar, N. Mathews, Formamidinium tin-based perovskite with low E_g for photovoltaic applications. *J. Mater. Chem. A* **3**, 14996–15000 (2015).
23. T. Yokoyama, D. H. Cao, C. C. Stoumpos, T.-B. Song, Y. Sato, S. Aramaki, M. G. Kanatzidis, Overcoming short-circuit in lead-free $CH_3NH_3SnI_3$ perovskite solar cells via kinetically controlled gas–solid reaction film fabrication process. *J. Phys. Chem. Lett.* **7**, 776–782 (2016).
24. M. H. Kumar, S. Dharani, W. L. Leong, P. P. Boix, R. R. Prabhakar, T. Baikie, C. Shi, H. Ding, R. Ramesh, M. Asta, M. Graetzel, S. G. Mhaisalkar, N. Mathews, Lead-free halide perovskite solar cells with high photocurrents realized through vacancy modulation. *Adv. Mater.* **26**, 7122–7127 (2014).
25. F. Hao, C. C. Stoumpos, P. Guo, N. Zhou, T. J. Marks, R. P. H. Chang, M. G. Kanatzidis, Solvent-mediated crystallization of $CH_3NH_3SnI_3$ films for heterojunction depleted perovskite solar cells. *J. Am. Chem. Soc.* **137**, 11445–11452 (2015).
26. N. Wang, Y. Zhou, M.-G. Ju, H. F. Garces, T. Ding, S. Pang, X. C. Zeng, N. P. Padture, X. W. Sun, Heterojunction-depleted lead-free perovskite solar cells with coarse-grained B-γ-$CsSnI_3$ thin films. *Adv. Energy Mater.* **6**, 1601130 (2016).
27. K. P. Marshall, M. Walker, R. I. Walton, R. A. Hatton, Enhanced stability and efficiency in hole-transport-layer-free $CsSnI_3$ perovskite photovoltaics. *Nat. Energy* **1**, 16178 (2016).
28. W. Ke, C. C. Stoumpos, J. L. Logsdon, M. R. Wasielewski, Y. Yan, G. Fang, M. G. Kanatzidis, TiO_2-ZnS cascade electron transport layer for efficient formamidinium tin iodide perovskite solar cells. *J. Am. Chem. Soc.* **138**, 14998–15003 (2016).
29. S. J. Lee, S. S. Shin, Y. C. Kim, D. Kim, T. K. Ahn, J. H. Noh, J. Seo, S. I. Seok, Fabrication of efficient formamidinium tin iodide perovskite solar cells through SnF_2–pyrazine complex. *J. Am. Chem. Soc.* **138**, 3974–3977 (2016).
30. W. Liao, D. Zhao, Y. Yu, C. R. Grice, C. Wang, A. J. Cimaroli, P. Schulz, W. Meng, K. Zhu, R.-G. Xiong, Y. Yan, Lead-free inverted planar formamidinium tin triiodide perovskite solar cells achieving power conversion efficiencies up to 6.22%. *Adv. Mater.* **28**, 9333–9340 (2016).
31. Space group: *I*2/*m*; lattice constants: a = 5.078(2) Å, b = 5.065(1) Å, c = 12.515(5) Å; β = 96.23(2)°; R_{obs} = 0.0470, wR_{obs} = 0.1096.
32. C. C. Stoumpos, M. G. Kanatzidis, Halide perovskites: Poor man's high-performance semiconductors. *Adv. Mater.* **28**, 5778–5793 (2016).
33. M. Liu, M. B. Johnston, H. J. Snaith, Efficient planar heterojunction perovskite solar cells by vapour deposition. *Nature* **501**, 395–398 (2013).
34. W. Ke, D. Zhao, C. R. Grice, A. J. Cimaroli, G. Fang, Y. Yan, Efficient fully-vacuum-processed perovskite solar cells using copper phthalocyanine as hole selective layers. *J. Mater. Chem. A* **3**, 23888–23894 (2015).
35. Q. Chen, H. Zhou, Z. Hong, S. Luo, H.-S. Duan, H.-H. Wang, Y. Liu, G. Li, Y. Yang, Planar heterojunction perovskite solar cells via vapor-assisted solution process. *J. Am. Chem. Soc.* **136**, 622–625 (2014).
36. N. J. Jeon, J. H. Noh, Y. C. Kim, W. S. Yang, S. Ryu, S. I. Seok, Solvent engineering for high-performance inorganic–organic hybrid perovskite solar cells. *Nat. Mater.* **13**, 897–903 (2014).
37. D. H. Cao, C. C. Stoumpos, O. K. Farha, J. T. Hupp, M. G. Kanatzidis, 2D homologous perovskites as light-absorbing materials for solar cell applications. *J. Am. Chem. Soc.* **137**, 7843–7850 (2015).
38. P. E. Blöchl, Projector augmented-wave method. *Phys. Rev. B* **50**, 17953–17979 (1994).
39. G. Kresse, J. Furthmüller, Efficient iterative schemes for ab initio total-energy calculations using a plane-wave basis set. *Phys. Rev. B* **54**, 11169–11186 (1996).
40. A. Stroppa, D. Di Sante, P. Barone, M. Bokdam, G. Kresse, C. Franchini, M. H. Whangbo, S. Picozzi, Tunable ferroelectric polarization and its interplay with spin–orbit coupling in tin iodide perovskites. *Nat. Commun.* **5**, 5900 (2014).
41. J. P. Perdew, K. Burke, M. Ernzerhof, Generalized gradient approximation made simple. *Phys. Rev. Lett.* **77**, 3865–3868 (1996).
42. V. Petříček, M. Dušek, L. Palatinus, Crystallographic computing system JANA2006: General features. *Z. Kristallogr. Cryst. Mater.* **229**, 345–352 (2014).

Acknowledgments

Funding: This work was supported in part by the Argonne-Northwestern Solar Energy Research Center, an Energy Frontier Research Center funded by the U.S. Department of Energy, Office of Science, and Office of Basic Energy Sciences under award DE-SC0001059. This work made use of the Engineering Product Innovation Center facility (Northwestern University's Atomic and Nanoscale Characterization Experimental Center), which has received support from the Materials Research Science and Engineering Center program (NSF DMR-1121262) at the Materials Research Center and the Nanoscale Science and Engineering Center (EEC-0118025/003), both programs of the NSF; the State of Illinois; and Northwestern University. **Author contributions:** W.K., C.C.S., and M.G.K. conceived the idea, designed the experiments, and wrote the manuscript. W.K. carried out film and device fabrication and characterization. C.C.S., W.K., L.M., and I.S. analyzed the data, synthesized the crystals, and

performed XRD, TGA, density, PL, and bandgap measurements. M.Z. assisted in device fabrication and characterization. J.L., D.S., and Y.Z. measured the NMR spectra and analyzed the data. O.Y.K. performed theory calculations. M.C. and M.R.W. conducted PL and TRPL measurements. All authors discussed the results and commented on the manuscript. M.G.K. supervised the project. **Competing interests:** The authors declare that they have no competing interests. **Data and materials availability:** All data needed to evaluate the conclusions in the paper are present in the paper and/or the Supplementary Materials. Additional data related to this paper may be requested from the authors.

Submitted 21 April 2017
Accepted 3 August 2017
Published 30 August 2017
10.1126/sciadv.1701293

Citation: W. Ke, C. C. Stoumpos, M. Zhu, L. Mao, I. Spanopoulos, J. Liu, O. Y. Kontsevoi, M. Chen, D. Sarma, Y. Zhang, M. R. Wasielewski, M. G. Kanatzidis, Enhanced photovoltaic performance and stability with a new type of hollow 3D perovskite {en}$FASnI_3$. *Sci. Adv.* **3**, e1701293 (2017).